Molecular Crystals and Liquid Crystals
Publication details, including instructions for authors and subscription information:
http://www.tandfonline.com/loi/gmcl20

Modeling Nematicon Propagation

Alessandro Alberucci [a] & Gaetano Assanto [a]
[a] NooEL, Nonlinear Optics and OptoElectronics Lab , University "Roma Tre" , Rome , Italy
Published online: 02 Apr 2013.

To cite this article: Alessandro Alberucci & Gaetano Assanto (2013) Modeling Nematicon Propagation, Molecular Crystals and Liquid Crystals, 572:1, 2-12, DOI: 10.1080/15421406.2012.763018

To link to this article: http://dx.doi.org/10.1080/15421406.2012.763018

Mol. Cryst. Liq. Cryst., Vol. 572: pp. 2–12, 2013

ISSN: 1542-1406 print/1563-5287 online
DOI: 10.1080/15421406.2012.763018

Modeling Nematicon Propagation

ALESSANDRO ALBERUCCI* AND GAETANO ASSANTO

NooEL, Nonlinear Optics and OptoElectronics Lab, University "Roma Tre", Rome, Italy

We discuss, both theoretically and numerically, the propagation of self-confined beams in uniaxial nematic liquid crystals. Our model accounts for optical anisotropy and goes beyond the perturbative regime, that is, it allows addressing the unique properties of nematicons, including their tunable nonlinearity, high nonlocality, and ability to spatial self-steer.

Keywords Liquid crystals; nonlinear optics; reorientational response; spatial solitons routing; spatial solitons

1. Introduction

Self-focusing of light beams in nematic liquid crystals (NLC) is an important current topic in the field of nonlinear optics [1–3]. When self-focusing in NLC becomes comparable with the natural tendency of two dimensional beams to diffract, they undergo self-trapping, that is, their width assumes a bounded value while propagating; such nonlinear wave packets in NLC are called nematicons [1,2]. Light self-focusing in NLC can occur via two main distinct mechanisms [4]: thermo-optic response [5] and reorientational nonlinearity [1,2]. The thermal nonlinearity is based on the dependence of the NLC refractive indices on temperature and the order parameter, whereas in the reorientational case the changes in the extraordinary refractive index are due to light-driven molecular rotation [4].

Historically, the pioneering work conducted by Braun and co-workers, who studied light filamentation in dye-doped NLC employing geometries subject to the Fréedericksz threshold [6], was revived by Warenghem and collaborators [7]. A step forward was made by Peccianti *et al.* who used voltage-biased cells to overcome the threshold and observed stable spatial solitons in two transverse dimensions [8]. The stabilization of (2+1)D nonlinearly self-trapped waves, normally unstable in Kerr media, can be ascribed to the highly nonlocality of NLC, the latter property supporting accessible solitons [9] even when spatially incoherent or multiwavelength [10,11]. Since then, several experiments have been conducted with nematicons, involving voltage-controlled angular steering via variations in walk-off [12], interaction between nematicons [13,14], deflection via localized perturbations [15], interactions with interfaces [16], all-optical logic gates [17–19], self-steering [20], and so on. From the theoretical/numerical point of view, a large number of articles available in the literature are based on perturbative assumptions [9,11,21–25], the latter hampering the proper description of the highly nonlinear regime and related effects, such

*Address correspondence to Alessandro Alberucci, Via della Vasca Navale 84, 00146 Rome, Italy. E-mail: alberucc@uniroma3.it

as self-steering via walk-off self-changes and the saturating character of the nonlinear response. Nonperturbative models were first introduced by McLaughlin and collaborators [26], but restricted to the experimental geometry studied by Braun *et al.* [6].

In this article, first we numerically compute the nematicon profile, revealing the nonperturbative features mentioned above and showing those features inherent to accessible solitons. Next, after introducing a simplified (1+1)D model for nonlinear light propagation, we numerically simulate the evolution of the optical wave packet accounting for actual sample and material limitations, such as losses. Then, we investigate how nematicons behave in the presence of inhomogeneities of the dielectric tensor, concluding with the interaction between two nematicons.

2. Nematicon Profile

Most NLC behave macroscopically as positive uniaxial crystals, with the optic axis coincident with the molecular director $\hat{n}$, in turn corresponding to the average direction of the molecules at a given point in space. We name $\varepsilon_{//}$ and $\varepsilon_{\perp}$ the two values assumed by the dielectric constant for electric fields polarized parallel and perpendicular to $\hat{n}$, respectively; we also define the dielectric anisotropy $\varepsilon_a = \varepsilon_{//} - \varepsilon_{\perp}$. The dielectric tensor $\overline{\overline{\varepsilon}}$, generally variable in space, is univocally determined by $\varepsilon_{//}$, $\varepsilon_{\perp}$, and the orientation of $\hat{n}$ via the expression $\varepsilon_{jk} = \varepsilon_{\perp}\delta_{jk} + \varepsilon_a n_j n_k$ $(j, k = x, y, z)$, with n_j being the Cartesian components of $\hat{n}$. Extraordinarily-polarized plane waves with wave vectors parallel to $\hat{z}$ are univocally associated to the extraordinary refractive index $n_e = \sqrt{\varepsilon_{yy} - \varepsilon_{yz}^2/\varepsilon_{zz}}$, determining their phase velocity, and to the walk-off angle $\delta = \arctan\left(\varepsilon_{yz}/\varepsilon_{zz}\right)$, the angle formed by the Poynting vector with the wave vector. Hereafter, we will assume that $\hat{n}$ lies in the plane yz, at an angle θ with $\hat{z}$, the latter taken positive when $yz > 0$. We will consider an input wave vector parallel to the axis z. Consistently with the assumed planar distribution of $\hat{n}$, we consider excitations of the NLC layer only with the extraordinary field component. If k_0 is the vacuum wave number, the light field can be completely described using the magnetic field $H_x = Ae^{ik_0 n_e(\theta_b)z}$, with $\theta_b(z)$ the director angle corresponding to the beam axis [27]. We also set $\theta = \theta_0 + \psi$, with θ_0 the director distribution in the absence of light and ψ the optical perturbation responsible for self-focusing. Thus, in the harmonic regime and in the paraxial limit, light beam propagation is governed by [27,28]:

$$2ik_0 n_e(\theta_b)\left(\frac{\partial A}{\partial z} + \tan\delta_b \frac{\partial A}{\partial y}\right) + D_y \frac{\partial^2 A}{\partial y^2} + \frac{\partial^2 A}{\partial x^2} + k_0^2 \Delta n_e^2 A = 0, \tag{1}$$

$$\nabla^2\psi + \frac{\varepsilon_0 \varepsilon_a Z_0^2}{4K n_e^2(\theta_b)\cos^2\delta_b}|A|^2 \sin\left[2(\theta_0 + \psi - \delta_b)\right] = 0, \tag{2}$$

where $\delta_b = \delta(\theta_b)$, K is a single elastic constant based on Frank's theory, $D_y = n_e^2(\theta_b)/\varepsilon_{zz}$ is the diffraction coefficient along y, Z_0 is the vacuum impedance, and $\Delta n_e^2 = n_e^2 - n_e^2(\theta_b)$ is an effective potential acting on the beam. In writing Eqs. (1 and 2) we assumed adiabatic variations in $\hat{n}$, such hypothesis comprising the assumption of a high nonlocal nonlinear response for ψ. The photonic potential Δn_e^2 is responsible for both light self-confinement and beam deflections related with wave vector rotations. The term proportional to the first derivative of A along y in Eq. (1) accounts for walk-off: when the angle $\theta_b(z)$ perceived by the beam varies due to θ_0 (linear changes on the dielectric properties of the sample) and ψ (nonlinear orientation, i.e., self-steering) the local slope of the beam trajectory

changes, even if the wave vector is unchanged. To account for self-steering via nonlinear changes in walk-off we introduce the parameter $c_\delta = \mathrm{d}\delta_b \big/ \mathrm{d}P\big|_{\theta_b}$, with P the beam power. In the nonlinear perturbative regime, that is, in the case $\psi << \theta_0$, the reorientational Eq. (2) can be linearized, providing an effective nonlocal Kerr coefficient $n_{2H}(\theta_0) = 2\gamma n_e^2(\theta_0) \tan\delta_0 \sin[2(\theta_0 - \delta_0)]$, having set $\delta_0 = \delta(\theta_0)$ [27].

3. Propagation of Single Nematicons in Homogeneous Samples

The first step in our analysis is to compute the profile of the nonlinear wave packet preserving its shape while propagating along z in an NLC layer, the latter taken homogeneous in the absence of optical perturbations. The solutions of Eqs. (1 and 2) strictly depend on the geometry of the interfaces bounding the NLC layer; in agreement with most experiments, we consider a planar cell of finite thickness L along x and infinitely extended in the plane yz. To account for nonlinear walk-off we make the ansatz $A = A_S(x, y - \tan\delta_b z)\exp(ik_0 n_{NL} z)$ and $\psi = \psi_S(x, y - \tan\delta_b z)$ for the envelope and the optical perturbation, respectively [28]. In this ansatz, we also consider a beam propagating in the cell mid-plane ($x = 0$) in order to avoid the insurgence of forces stemming from asymmetric boundary conditions [29]. Moreover, hereby we restrict to the lowest order nematicon, that is, a soliton with a bell-shaped transverse profile [30]. Finally, all the numerical results were obtained for a wavelength of 1064 nm and with reference to the commercial NLC mixture known as E7.

Substitutions into systems (1 and 2) yield a nonlinear eigenvalue problem with solutions – dependent on beam power P – which can be solved iteratively and consisting of the two transverse distributions $A_S(x, y, P)$ (see Fig. 1(a)) and $\psi_S(x, y, P)$ (see Fig. 1(b)), with the two scalar values $\delta_b(P)$ (Fig. 1(d)) and $n_{NL}(P)$ (Fig. 1(g)), the latter accounting for power-dependent variations in the nematicon propagation constant. If the

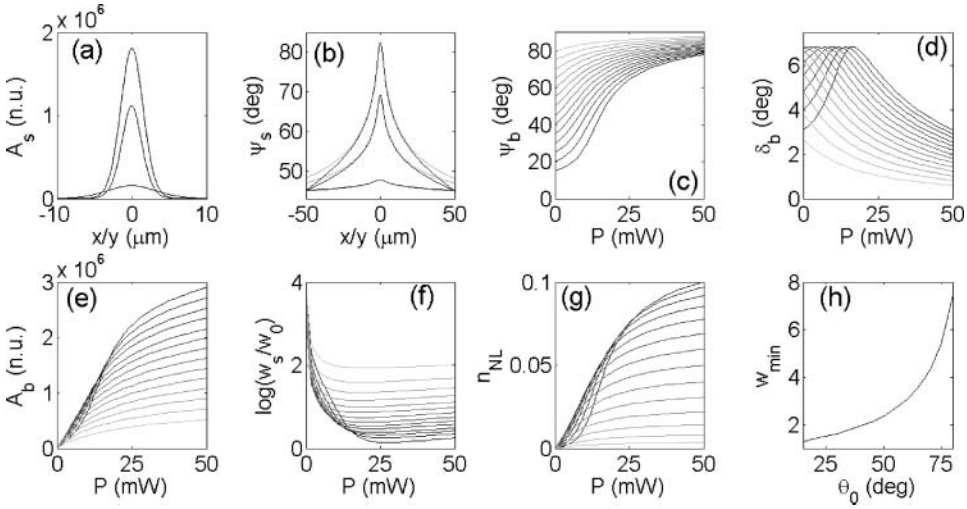

Figure 1. (a) Nematicon profile and (b) the corresponding optical perturbation versus x (black line) and y (gray lines) for $\theta_0 = 45^\circ$; the input powers are $P = 1.8$, 16, and 50 mW, from bottom to top curves, respectively. Behavior of (c) ψ_b, (d) δ_b, (e) A_b, (f) nematicon waist in log scale, and (g) n_{NL} versus input power; each curve corresponding to a different value of θ_0, starting from 15° (darkest line) to 80° (lightest line) in steps of 5°. The reference waist w_0 is equal to 1 μm. (h) Minimum nematicon waist versus initial angle θ_0. Here, we considered a cell of thickness $L = 100$ μm.

nematicon waist w is much smaller than the cell thickness L, the soliton transverse profile is close to a Gaussian (in agreement with the highly nonlocal model [31]), with nearly equal profiles along x and y despite the anisotropy due to the medium birefringence (D_y is close to 1, see [32]) and the anisotropic boundary conditions (Fig. 1(a)). The cylindrical symmetry breaks up when the size of the photonic wave packet becomes comparable to L. The distribution of ψ_s confirms our physical interpretation: the optical perturbation goes as the Green function of Eq. (2) in the given geometry [33], except for a small region close to the beam axis where it takes a quasiparabolic shape, with differences along x and y arising only at the wings (Fig. 1(b)). As visible in the plot of ψ_s peak (Fig. 1(c)), the nonlinear response saturates for large powers and its general behavior depends strongly on the initial angle θ_0. Graphs of the nematicon walk-off δ_b demonstrate how the beam trajectory can change with light power, the variation with P strictly depending on θ_0 (Fig. 1(d)). Figures 1(e and f) describe the trend of the nematicon peak A_b and waist w versus power: due to the saturable character of the reorientational nonlinearity, the waist reduction versus power is halted, with the location of the inversion (i.e., where $dw/dP = 0$) varying with θ_0. Figure 1(g) shows how n_{NL} monotonically grows with P, thus stating the stability of the nematicon according to the Vakhitov–Kolokolov criterion [34]. Finally, Fig. 1(h) shows the smallest waist obtainable for each value of θ_0: the narrowest nematicons can be excited for low initial angles, although the nonlinearity in the perturbative regime reaches its maximum for $\theta_0 \approx 45^\circ$. In other words, at high powers it is important to account for nonperturbative effects, as demonstrated by the noticeable asymmetry in nematicon behavior for initial angles equally distant from the perturbative optimum $\theta_0 = 45^\circ$ [32].

Analytically, an approximated closed-solution can be derived in the highly nonlocal limit assuming that ψ_S is cylindrically symmetric and follows a parabolic trend, that is, $\psi_S = \psi_b - \psi_2\left(x^2 + y^2\right)$ with $\psi_2 = [\varepsilon_0\varepsilon_a/(4K)]\sin[2(\theta_b - \delta_b)]|A_b|^2/4$ [9]. In this limit nematicons are accessible solitons, and their existence curve in the plane waist power can be derived from known results for the quantum harmonic oscillator, yielding $n_2(\theta_b)\, P_s w_s = 8\pi n_e(\theta_b)/\left(k_0^2 Z_0\right)$.

The calculation of nematicon profiles alone is not sufficient to characterize light self-confinement in NLC: important information derives from the propagation problem, that is, the computation of the beam profile when the input excitation is given. It has been demonstrated how, owing to the high nonlocality of the reorientational nonlinearity, self-trapped waves take the general form of breathing wave packets, that is, spatially localized beams with waist (and peak intensity) oscillating along propagation [9,27]. Such numerical data are fundamental for the comparison with experimental observations, where the impinging intensity is the parameter under control.

The best approach to simulate light propagation is to employ the Beam Propagation Method (BPM). Our numerical scheme encompasses the computation of light evolution for a given director distribution using Eq. (1); then, the intensity profile is inserted into Eq. (2) and, via a standard relaxation algorithm, the director profile in the NLC layer is calculated. Such procedure is iterated until convergence is achieved. The full three-dimensional (3D) simulation of systems (1 and 2) is time consuming because of the slow convergence of the 3D relaxation code. The underlying physics, however, can be adequately modeled resorting to a simplified (1+1)D model considering light propagation only in the mid-plane $x = 0$. Equation (1) can be directly employed eliminating the derivatives along x, whereas the reorientational Eq. (2) can be replaced by [27,28]

$$\nabla_{yz}^2\psi - \left(\frac{\pi}{L}\right)^2\psi + \frac{\varepsilon_0\varepsilon_a Z_0^2}{4Kn_e^2(\theta_b)\cos^2\delta_b}|A|^2\sin\left[2\left(\theta_0 + \psi - \delta_b\right)\right] = 0. \tag{3}$$

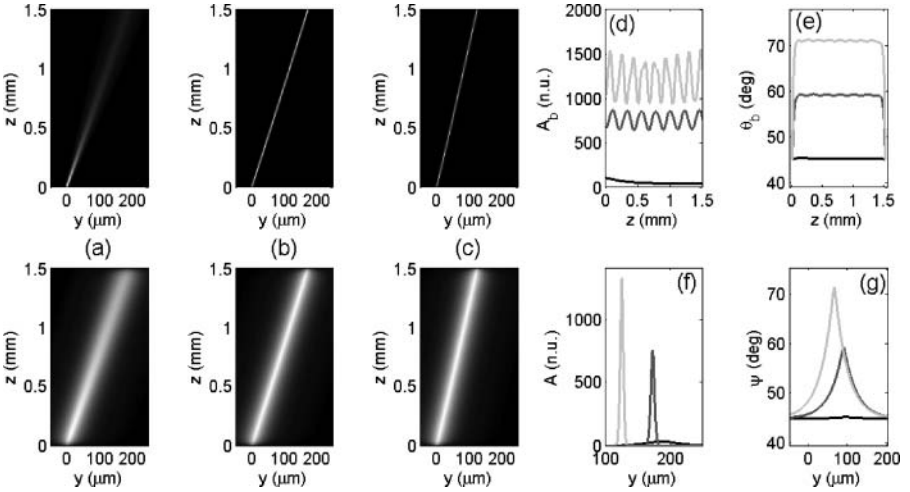

Figure 2. Light evolution on the plane yz for (a) $P = 50$ μW, (b) 2 mW, and (c) 5 mW; top panels show the intensity profile, bottom panels graph the distribution of θ. Behavior of (d) the peak of the field and (e) director angle distribution versus propagation coordinate z; powers are as in (a–c), with the lightest line corresponding to the highest power. (f) Output intensity distribution for $z = 1.5$ mm and (g) optical perturbation in the plane $z = 0.75$ mm; the color code is the same as in (d and e). Here, $\theta_0 = 45^\circ$ and the input waist is 5 μm.

Equation (3) has the advantage of maintaining the original nonlocal range given by L (see Fig. 1) while drastically shortening the numerical computation. In comparing with experiments or full 3D numerical simulations, however, we have to include a power fit-parameter [27]. We note that Eq. (3) allows the correct computation of changes in nematicon trajectory (both of linear and nonlinear origins) because it accounts for the derivatives along z, at variance with previous perturbative models requiring straight propagation along a direction defined *a priori* [9,11,35]. In the simulations hereafter, we will always take a Gaussian profile for the input beam(s) and a cell thickness L of 100 μm, the latter being a convenient value for comparisons with experimental results.

An example of numerical computation in (1+1)D is in Fig. 2; the sample extends for 1.5 mm along z; at input ($z = 0$) and output sections ($z = 1.5$ mm), we assume strong anchoring and set $\theta = \theta_0$. As input power is increased, the beam self-confines, with its waist undergoing quasiperiodic oscillations along z as expected from accessible solitons (Figs. 2(a–d)) [9,31]. Moreover, the beam changes its own path through nonlinear variations in walk-off (see Figs. 2(f and g)), resulting in nematicons propagating along straight lines in the plane yz, with a slope depending on input power and comprised between 0° and 7°, the latter corresponding to the maximum walk-off for the chosen NLC mixture and wavelength. The plots of ψ in yz (Figs. 2(a–c)) demonstrate how our model conserves both the degree of nonlocality and the profile of the perturbation across y (compare Fig. 1(b) with Figs. 2(a–c) and (g)). Figure 2(e) plots the peak of the director angle versus z: since Eq. (3) conserves nonlocality along z, θ_b is a smooth function (setting the θ derivative along z equal to zero implies a local response in that direction). Under the local approximation we get $\psi_2 \propto w^{-2}$ (see above), implying unphysical fast oscillations of the director distribution across z. inducing in turn strong aperiodic breathing for large powers [36].

Nematicon profiles in Figs. 1 and 2 are computed in the absence of optical losses. In actual experiments losses are unavoidable due to the strong scattering typical of the nematic

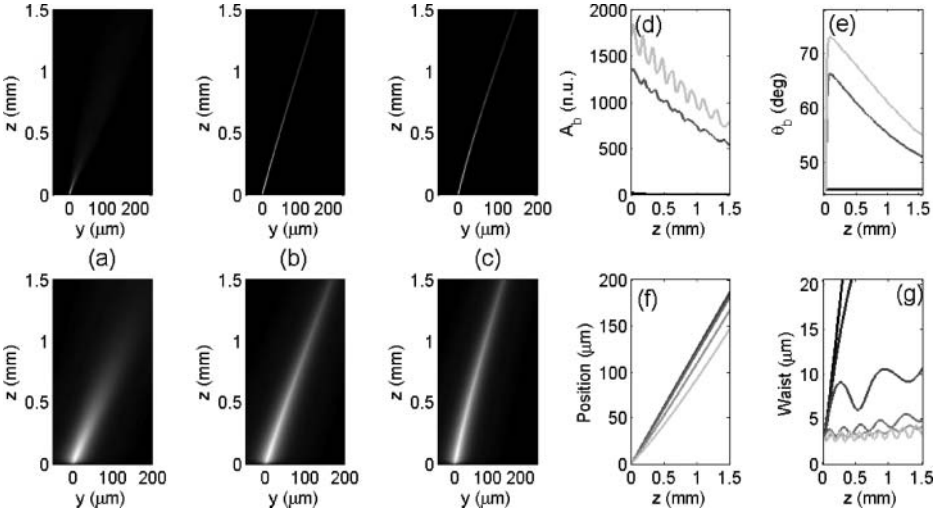

Figure 3. Light beam evolution in the plane yz for (a) $P = 1$ mW, (b) 3 mW, and (c) 5 mW considering an attenuation of 5 cm^{-1}; top and bottom panels show intensity and director angle distributions, respectively. Peak of (d) the field and (e) the director angle versus z; powers are as in (a–c), with the lightest lines corresponding to the largest powers. Beam (f) trajectory and (g) waist versus z; from the darkest to the lightest curve the power is 1 μW, 200 μW, 500 μW, 1.5 mW, 3 mW, and 5 mW, respectively. Here, $\theta_0 = 45^\circ$ and the input waist is 3 μm.

phase, with values as large as 0.5 cm^{-1} in the infrared, thus playing a not negligible role. Figures 3(a–c) shows nematicon evolution in the presence of losses; the BPM grid is taken large enough to avoid spurious effects from boundaries [29]. Since the effective power decreases as z increases, we expect nonlinear effects, that is, the reorientational torque, to diminish as well, leading to a negligible ψ_b for large enough propagation distances; Figures 3(d and e) illustrates the decrease along z of the maximum optical field and the nonlinear perturbation, respectively. The effects on nematicon evolution are apparent: nematicons, at variance with Fig. 2, now move in a warped trajectory, with an output slope given by linear walk-off δ_0 (see Fig. 3(f)). The losses affect self-focusing in a similar way: a reduction is observed in the spatial trapping of light, leading to a continuous variation in breathing cycles (see Fig. 3(g)).

We remark that, for the sake of conciseness, we did not analyze the dependence of light self-confinement on θ_0 via BPM simulations: the behavior is analogous to the dynamics of the nematicon profile as plotted in Fig. 1. An exhaustive discussion of this case can be found in Ref. [27].

4. Nematicon Interaction with Localized Inhomogeneities

In Section 3, we dealt with single nematicons propagating in an initially homogeneous NLC layer. The simplified (1+1)D model, however, is also able to describe nonlinear light propagation when θ_0 is spatially inhomogeneous, assuming the variations are slow with respect to the beam waist. To get started, let us consider a localized defect in director orientation, as given by $\theta_0 = \theta_{in} + \Delta\theta \exp\left[-(y - y_D)^2/w_D^2 - (z - z_D)^2/w_D^2\right]$. In this section we will neglect propagation losses.

We expect to observe two different evolution regimes according to the ratio of beam waist w and defect width w_D [37,38]: when the beam is much narrower than the defect,

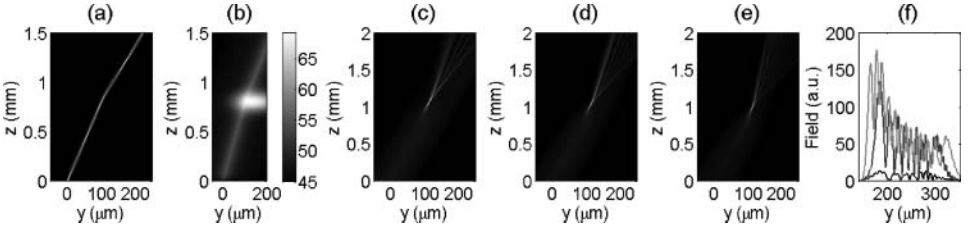

Figure 4. (a) Intensity and (b) director distribution of a nematicon with initial waist of 3 μm and power of 1 mW interacting with a circular Gaussian defect located in ($y_D = 150$ μm, $z_D = 800$ μm) and of width $w_D = 100$ μm. Field profiles of nematicons of (c) $P = 0.1$ mW, (d) $P = 5$ mW, and (e) $P = 10$ mW interacting with a circular defect in ($y_D = 80$ μm, $z_D = 800$ μm) and with $w_D = 30$ μm; the input beam waist is 60 μm. (f) Intensity profiles versus y evaluated in $z = 2$ mm, corresponding to the cases plotted in panels (c)–(e), from the darkest to the lightest line, respectively. Here, we took $\theta_{in} = 45^\circ$ and $\Delta\theta = 20^\circ$.

the nematicon behaves as a particle, preserving itself as a single-hump localized structure; in the opposite limit the nematicon behaves as a wave, forming fringes due to interference between different portions of the scattered wave.

Figure 4 confirms our qualitative predictions: narrow nematicons (see Figs. 4(a and b)) preserve their transverse profile, undergoing deflection due to the index gradient introduced by the linear defect [39] (in the case shown an effective force is pushing the nematicon toward larger y). Conversely, for nematicons of waist comparable with the defect width, the differential phase delay encompassed by each portion of the wave packet induces interference effect and, in turn, fringes in the far field. At low powers (Fig. 4(c)) the fringe distribution is symmetric with respect to the propagation direction, whereas at large powers each fringe self-focuses separately into a filament (Fig. 4(d)). If power is further increased, the filaments begin to interact with one another (Fig. 4(e)), with highest intensities toward small y (Fig. 4(f)).

Another interesting case is that of nematicons impinging on a linear interface, that is, an NLC region with a uniform θ_0 along z and a monotonic (increasing or decreasing depending on the sign of $\Delta\theta$) distribution versus y [40]. We study grazing incidence, that is, beams with input wave vector almost along z. The beam is launched in $y = -100$ μm; the graded interface is centered in $y = 0$ and extends from -50 μm to 50 μm, with an overall width equal to L and, therefore, comparable with the nonlocality range. Moreover, we assume for θ_0 a linear distribution, going from $\theta_1 > 0$ for $y < -L/2$ to $\theta_2 > 0$ for $y > L/2$; hence, the reorientation barrier is $\Delta\theta = \theta_2 - \theta_1$ [16,40]. Owing to walk-off, the wave packet penetrates the barrier even if its phase fronts are normal to z. For $\Delta\theta < 0$, a net force stemming from the index gradient repels the beam *pushing* light toward negative y, for both diffracting (Figs. 5(a) and (e)) and self-confined wave packets (Figs. 5(b) and (f)). For $\Delta\theta > 0$, the force changes sign and the wave vector bends toward positive y, allowing the beam to cross the interface, both in the linear (Figs. 5(c) and (g)) and the nonlinear regimes (Figs. 5(d) and (h)). Noteworthy, due to the adiabatic nature of the interface as compared to the wavelength and the beam waist, a nematicon preserves self-confinement and remains a single entity.

5. Interaction Between Two Nematicons

In this section, we address the interaction between two coplanar nematicons launched parallel (for the case of skew nematicons see [41,42]) in a lossy NLC layer and with the same input waist and power. We assume the two beams are coherent, with initial phase

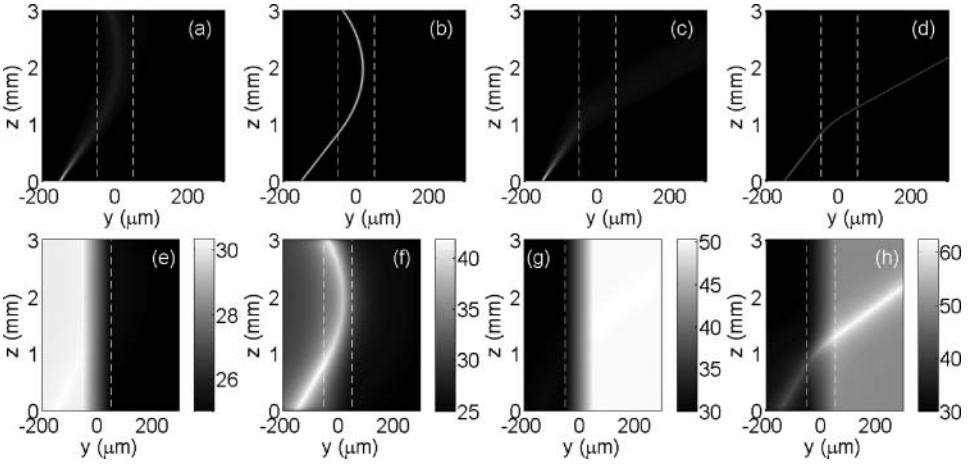

Figure 5. Grazing incidence of a nematicon upon a linear interface: (a, b, e, and f) total internal reflection and (c, d, g, and h) refraction. The input power is 0.1 mW in (a, c, e, and g) and 3 mW in (b, d, f, and h). In the reflected case, it is $\Delta\theta = -5^\circ$, whereas in the transmitted case it is $\Delta\theta = 20^\circ$. Here, we consider $L = 100$ μm and $\theta_1 = 30^\circ$, the dielectric interface is graded over a thickness L; the dashed white lines indicate the boundaries of the interface.

delay ϕ and separation d, that is, an excitation of the form

$$A(y, z = 0) = A_0 \left\{ \exp\left[-(y - d/2)^2 \Big/ w_{in}^2 \right] + \exp(i\phi) \exp\left[-(y + d/2)^2 \Big/ w_{in}^2 \right] \right\}.$$

Figure 6 plots the numerical results on the collisional interaction when the two beams are in phase at the input and for increasing excitation, from left to right. Even

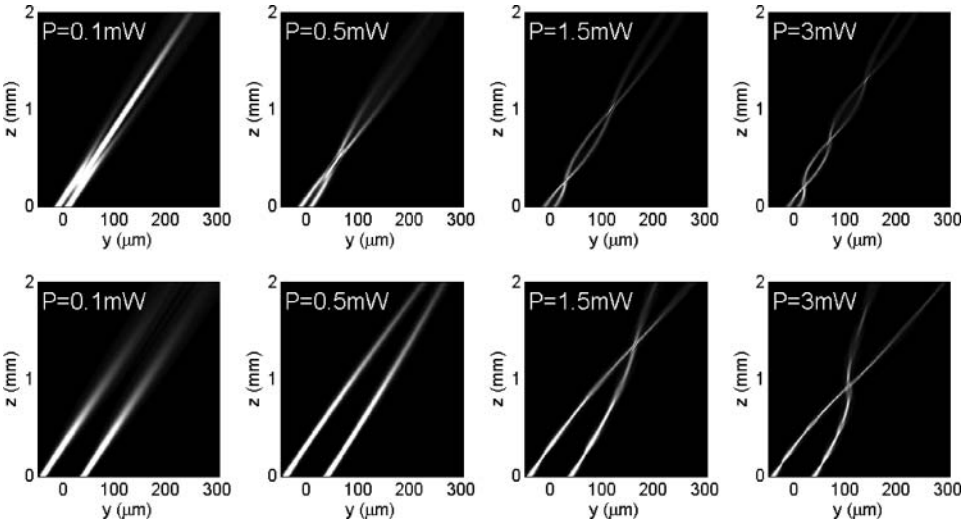

Figure 6. Interaction between two nematicons carrying the same power for $d = 20$ μm (top row) and $d = 80$ μm (bottom row). The input waist w_{in} is 7 μm, the cell thickness L is 100 μm, and θ_0 is 45°.

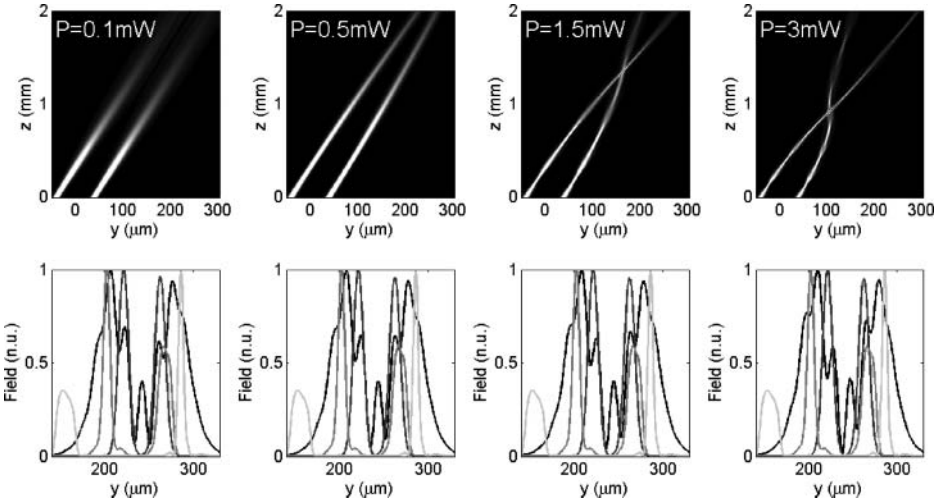

Figure 7. Top: interaction between two identical nematicons in the plane yz for $\phi = 90^\circ$ $d = 80$ μm, $\theta_0 = 45^\circ$, and various input powers. Bottom: transverse intensity profiles at $z = 2$ mm for $\varphi = 0^\circ,\ 30^\circ,\ 45^\circ,$ and 90°, from left to right, respectively; in each graph the powers are as in the top panels, the largest corresponding to the lightest line. The profiles versus y are scaled with respect to the peak.

if the two intensity distributions do not overlap at the input, the nematicon are able to attract each other due to the nonlocality, the latter responsible for a light-induced index well much wider than the beams themselves [43]. For a given initial separation d, the larger is the power the stronger is the attraction between the two nematicons, as proven

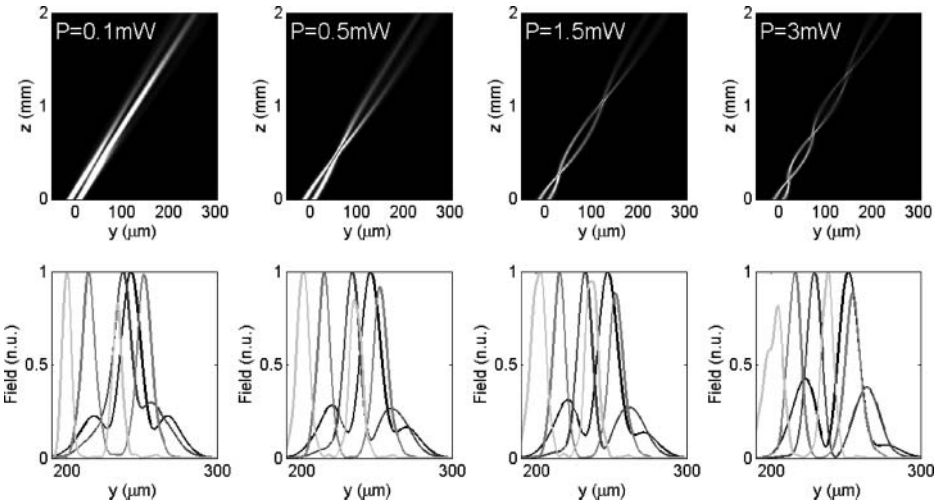

Figure 8. Top: interaction between two identical nematicons in the plane yz for $\phi = 90^\circ$ $d = 20$ μm, $\theta_0 = 45^\circ$, and various input powers. Bottom: intensity transverse profiles in $z = 2$ mm for $\varphi = 0^\circ,\ 30^\circ,\ 45^\circ,$ and 90°, from left to right, respectively; in each graph the powers are as in the top panels, the largest corresponding to the lightest line. The profiles versus y are scaled with respect to the peak.

by the number of the crossing points and their distance from the input section $z = 0$ [43]. Noticeably, the aperiodic interleaving is mainly caused by losses, similarly to the breathing of isolated nematicons. The binding force between nematicons decreases for increasing d [43] (compare top and bottom panels in Fig. 6), with a negligible entanglement when $d \approx L$.

The next step is the study of the interaction dynamics versus initial phase delay. Figure 7 shows the computed results for $d = 80$ μm. When self-focusing is strong, no appreciable differences are observed as ϕ changes, whereas for diffracting beams the detailed intensity distribution changes with ϕ, as expected. An asymmetry in the intensity distribution even for $\phi = 0$ (the input has an even parity) is attributed to the anisotropy of the medium, that is, to walk-off. A dependence on ϕ is observed for a reduced initial separation d: Fig. 8 shows the same quantities plotted in Fig. 7 but for a smaller $d = 20$ μm. In this case, the power redistributes between the two output peaks even at high powers, leading to both displacement in the nematicon positions and changes in the power carried by each one of them. Remarkably, the nematicons attract for every ϕ owing to the high nonlocality: such behavior strongly differs from that of (local) Kerr-like media, where the phase delay between two solitons can produce attraction or repulsion or exchange of energy between the two self-confined wave packets [34,44,45].

6. Conclusions

We modeled nematicons accounting for the strong anisotropic nonlinear response of NLCs. First, we numerically solved the nonlinear eigenvalues problem in the full (2+1)D geometry, finding the profile of shape-preserving fundamental nematicons and addressing its dependence on the rest angle of the director. We also demonstrated nonperturbative effects, such as self-steering and saturation in the nonlinearity. Then, we investigated planar propagation of nematicon for a given input profile via a simplified (1+1)D model. In such a way, we analyzed the behavior of self-steering and breathing, that is, nematicon undergoing variation in waist along propagation, addressing the role of losses in actual experiments. We simulated the interaction between nematicons and spatial inhomogeneities in the dielectric tensor, both in the presence of localized defects and of adiabatic dielectric interfaces, demonstrating nematicon deflection via perturbations. Finally, we investigated the in-plane interaction between nematicons, focusing on its dependence on excitation, initial beam separation, and relative phase.

Acknowledgments

A. A. thanks “Regione Lazio” for financial support as well as the “Roma Tre” Internationalization program.

References

[1] Peccianti, M., & Assanto, G. (2012). *Phys. Rep.*, *516*, 147–208.
[2] Assanto, G. (2012). *Nematicons: Spatial Optical Solitons in Nematic Liquid Crystals*. Wiley: New York.
[3] Assanto, G., Fratalocchi, A., & Peccianti, M. (2007). *Opt. Express.*, *15*, 5248–5259.
[4] Simoni, F. (1997). *Nonlinear Optical Properties of Liquid Crystals*. World Scientific: Singapore.
[5] Derrien, F., Henninot, J. F., Warenghem, M., & Abbate, G. (2000). *J. Opt. A: Pure Appl. Opt.*, *2*, 332–337.
[6] Braun, E., Faucheux, L. P., & Libchaber, A. (1993). *Phys. Rev. A.*, *48*, 611–622.

[7] Warenghem, M., Henninot, J. F., Derrien, F., & Abbate, G. (2002). *Mol. Cryst. Liq. Cryst.*, *373*, 213–225.
[8] Peccianti, M., Assanto, G., De Luca, A., Umeton, C., & Khoo, I. C. (2000). *Appl. Phys. Lett.*, *77*, 7–9.
[9] Conti, C., Peccianti, M., & Assanto, G. (2004). *Phys. Rev. Lett.*, *92*, 113902.
[10] Peccianti, M., & G. Assanto, G. (2001). *Opt. Lett.*, *26*, 1791–1793.
[11] Alberucci, A., Peccianti, M., Assanto, G., Dyadyusha, A., & Kaczmarek, M. (2006) *Phys. Rev. Lett. 97*, 153903.
[12] Peccianti, M., Conti, C., Assanto, G., De Luca, A., & Umeton, C. (2004). *Nature.*, *432*, 733–737.
[13] Peccianti, M., Brzdiekwicz K., & Assanto, G. (2002). *Opt. Lett.*, *27*, 1460–1462.
[14] Hu, W., Zhang, T., Guo, Q., Xuan, L., & Lan, S. (2006). *Appl. Phys. Lett.*, *89*, 071111.
[15] Pasquazi, A., Alberucci, A., Peccianti, M., & Assanto, G. (2005). *Appl. Phys. Lett.*, *87*, 261104.
[16] Piccardi, A., Alberucci, A., Barboza, R., Buchnev, O., Kaczmarek, K., & Assanto, G. (2012). *Appl. Phys. Lett.*, *100*, 251107.
[17] Peccianti, M., Conti, C., Assanto, G., De Luca, A., & Umeton, C. (2002). *Appl. Phys. Lett.*, *81*, 3335–3337.
[18] Serak, S. V., Tabiryan, N. V., Peccianti, M., & Assanto, G. (2006). *IEEE Photon. Techn. Lett.*, *18*, 1287–1289.
[19] Piccardi, A., Alberucci, A., Bortolozzo, U., Residori, S., & Assanto, G. (2010). *Appl. Phys. Lett.*, *96*, 071104.
[20] Piccardi, A., Alberucci, A., & Assanto, G. (2010). *Appl. Phys. Lett.*, *96*, 061105.
[21] Conti, C., Peccianti, M., & Assanto, G. (2005). *Phys. Rev. E.*, *72*, 066614.
[22] Rasmussen, P. D., Bang, O., & Krolikowski, W. (2005). *Phys. Rev. A.*, *72*, 066611.
[23] Hu, W., Ouyang, S., Yang, P., Guo, Q., & Lan, S. (2008). *Phys. Rev. A.*, *77*, 033842.
[24] Assanto, G., Skuse, B., & Smyth, N. F. (2010). *Phys. Rev. A.*, *81*, 063811.
[25] Assanto, G., Minzoni, A. A., Smyth, N. F., & Worthy, A. (2010). *Phys. Rev. A.*, *82*, 053843.
[26] McLaughlin, D. W., Muraki, D. J., Shelley, M. J., & Wang, X. (1995). *Physica D.*, *88*, 55–81.
[27] Alberucci, A., Piccardi, A., Peccianti, M., Kaczmarek, M., & Assanto, G. (2010). *Phys. Rev. A.*, *82*, 023806.
[28] Alberucci, A., & Assanto, G. (2010). *Opt. Lett.*, *35*, 2520–2522.
[29] Alberucci, A., Peccianti, M., & Assanto, G. (2007). *Opt. Lett.*, *32*, 2795–2797.
[30] Izdebskaya, Y. V., Desyatnikov, A. S., Assanto, G., & Kivshar, Y. S. (2011). *Opt. Lett.*, *36*, 184–186.
[31] Snyder, A.W., & Mitchell, D.J. (1997), *Science.*, *276*, 1538–1541.
[32] Alberucci, A., Piccardi, A., & Assanto, G. (2012). *Mol. Cryst. Liq. Cryst.*, *558*, 2–11.
[33] Alberucci, A., & Assanto, G. (2007). *J. Opt. Soc. Am. B.*, *24*, 2314–2320.
[34] Kivshar, Y. S., & Agrawal, G. P. (2003). *Optical solitons*. Academic: San Diego.
[35] Minzoni, A. A., Sciberras, L. W., Smyth, N. F., & Worthy, A. (2011). *Phys. Rev. A.*, *84*, 043823.
[36] Alberucci, A., & Assanto, G. (2007). *J. Nonl. Opt. Phys. Mat.*, *16*, 295–305.
[37] Jisha, C. P., Alberucci, A., Lee, R.-K., & Assanto, G. (2011). *Opt. Lett.*, *36*, 1848–1850.
[38] Alberucci, A., Assanto, G., Minzoni, A. A., & Smyth, N. F. (2012). *Phys. Rev. A.*, *85*, 013804.
[39] Alberucci, A., Piccardi, A., Bortolozzo, U., Residori, S., & Assanto, G. (2010). *Opt. Lett.*, *35*, 390–392.
[40] Barboza, R., Alberucci A., & Assanto, G. (2011). *Opt. Lett.*, *36*, 2725–2727.
[41] Fratalocchi, A., Piccardi, A., Peccianti, M., & Assanto, G. (2007) *Opt. Lett.*, *32*, 1447–1449.
[42] Fratalocchi, A., Piccardi, A., Peccianti, M., & Assanto, G. (2007). *Phys. Rev. A.*, *75*, 063835.
[43] Kwasny, M., Piccardi, A., Alberucci, A., Peccianti, M., Kaczmarek, M., Karpierz, M., & Assanto, G. (2011). *Opt. Lett.*, *36*, 2566–2568.
[44] Stegeman, G. I., & Segev, M. (1999). *Science*, *286*, 1518–1523.
[45] Pasquazi, A., Stivala, S., Assanto, G., Gonzalo, J., & Solis, J. (2008). *Phys. Rev. A.*, *77*, 043808.